WWLLN lightning and satellite microwave radiometrics at 37 to 183 GHz: Thunderstorms in the broad tropics

N. N. Solorzano[1], J. N. Thomas[2,3,4], M. L. Hutchins[4], and R. H. Holzworth[4]

[1]Department of Physics, DigiPen Institute of Technology, Redmond, Washington, USA, [2]NorthWest Research Associates, Redmond, Washington, USA, [3]Department of Electrical and Computer Engineering, DigiPen Institute of Technology, Redmond, Washington, USA, [4]Department of Earth and Space Sciences, University of Washington, Seattle, Washington, USA

Abstract We investigate lightning strokes and deep convection through the examination of cloud-to-ground (CG) lightning from the World Wide Lightning Location Network (WWLLN) and passive microwave radiometer data. Microwave channels at 37 to 183.3 GHz are provided by the Tropical Rainfall Measuring Mission satellite (TRMM) Microwave Imager (TMI) and the Special Sensor Microwave Imager/Sounder (SSMIS) on the Defense Meteorological Satellite Program (DMSP) satellite F16. The present study compares WWLLN stroke rates and minimum radiometer brightness temperatures (Tbs) for two Northern Hemisphere and Southern Hemisphere summers (2009–2011) in the broad tropics (35°S to 35°N). To identify deep convection, we use lightning data and Tbs derived from all channels and differences in the Tbs (ΔTbs) of the three water vapor channels near 183.3 GHz. We find that stroke probabilities increase with increasing Tb depressions for all frequencies examined. Moreover, we apply methods that use the 183.3 GHz channels to pinpoint deep convection associated with lightning. High lightning stroke probabilities are found over land regions for both intense and relatively weak convective systems, although the TMI 85 GHz results should be used with caution as they are affected by a 7 km gap between the conical scans. Over the ocean, lightning is associated mostly with larger Tb depressions. Generally, our results support the noninductive thundercloud charging mechanism but do not rule out the inductive mechanism during the mature stages of storms. Lastly, we present a case study in which lightning stroke rates are used to reconstruct microwave radiometer Tbs.

1. Introduction

In this investigation, we use 2 years of data from the World Wide Lightning Location Network (WWLLN), a ground-based, global network that continually measures lightning strokes and a data set of passive microwave radiometer observations comprising frequencies between 37 and 183.3 GHz. The radiometer data are from two satellite platforms: the Tropical Rainfall Measuring Mission (TRMM) Microwave Imager (TMI) that provides brightness temperature (Tb) radiances at 37 and 85 GHz and the Special Sensor Microwave Imager/Sounder (SSMIS) on Defense Meteorological Satellite Program (DMSP) satellite F16 that provides radiances at 91.7, 150, and 183.3 GHz. The goals of this analysis are to describe convection within the broad tropics (from 35°S to 35°N) in terms of cloud-to-ground lightning stroke rate and microwave radiometer data and therefore study the relationships between lightning and cloud Tb characteristics, particularly ocean/land contrasts. We address the following questions:

1. Are lightning stroke rates and stroke probabilities higher for areas of deep convection identified using microwave radiometer techniques, particularly the 183.3 GHz channels used by *Hong and Heygster* [2008] and *Wang et al.* [1997]?
2. What are the land/ocean differences in these results?
3. What can be inferred about cloud hydrometeors, lightning rates, and cloud charging mechanisms?
4. Can these lightning and radiometer results be used to reconstruct Tbs to some extent in a case study?

We extend the results of many earlier studies [e.g., *Petersen et al.*, 2005; *Liu et al.*, 2011] that investigated global lightning and radiometer data from satellites, such as Lightning Imager Sensor (LIS) on TRMM or the Optical Transient Detector. One unique aspect of our work is that we use data from a ground-based lightning network (WWLLN), rather than satellite measurements. Our analysis also includes radiometric frequencies not typically compared with lightning observations, such as the 150 and 183.3 GHz channels on SSMIS. Additionally, we investigate dual-frequency Tbs and lightning probabilities, confirming and expanding

previous findings and presenting a new analysis with the water vapor channels (183.3 GHz). Finally, we present a case study with the goal of addressing question 4. The paragraphs below in this section contain a review of passive microwave Tbs, focusing on methods to investigate deep convection. We later describe the connections between Tbs, convection intensity, and lightning production.

There are tight links between lightning, convection, and cloud hydrometeor properties such as distribution, type, and mass [e.g., *Toracinta et al.*, 2002], which are related to passive microwave brightness temperatures (Tbs) [e.g., *Zipser et al.*, 2006; *Hong and Heygster*, 2008]. High concentrations of hydrometeors can be identified by increased radar reflectivity and decreased passive microwave Tbs in the mixed-phase region of a thundercloud (located around 0°C to −40°C) [e.g., *Cecil and Zipser*, 2002]. Numerous investigations have found high correlations between lightning flash rate and precipitation-sized ice mass or ice mass-related parameters, such as ice water path [e.g., *Cecil and Zipser*, 2002; *Petersen et al.*, 2005; *Latham et al.*, 2007; *Deierling and Petersen*, 2008; *Pessi and Businger*, 2009]. Moreover, lightning rates are well correlated with updraft velocities above a threshold of approximately 5 m/s in the mixed-phase environment [e.g., *Deierling and Petersen*, 2008].

Convection intensities and hydrometeor distributions have been described in terms of Tbs derived from passive microwave channels, with the frequent use of ice-scattering signatures. Passive microwave measurements are often used to investigate the cloud environment because, except for thin cirrus clouds, visible and infrared techniques tend to be most sensitive to the cloud top, whereas the entire, diverse hydrometeor collection in the cloud modulates microwave radiation [e.g., *Deeter and Evans*, 2000]. Visible and infrared radiation are sensitive to the visible optical depth, which is proportional to the projected particle area, whereas microwave wavelengths above 37 GHz are sensitive to higher moments of the particle size distribution and hence larger ice particles, presenting Tb depressions due to frozen hydrometeors [e.g., *Spencer et al.*, 1983; *Evans and Stephens*, 1995; *Deeter and Evans*, 2000].

Tbs at 37 to 183.3 GHz are depressed via scattering of upwelling radiation by liquid and frozen cloud hydrometeors [e.g., *Wu and Weinman*, 1984]. Each frequency has different scattering properties, and higher frequencies are generally more sensitive to smaller particles than lower frequencies. Although supercooled water in the mixed-phase region is required for charge separation [e.g., *Takahashi*, 1984], some model results [e.g., *Vivekanandan et al.*, 1991] suggest that supercooled water emissions increase Tbs in the 37–150 GHz range, masking the scattering signal from graupel at the same level [e.g., *Toracinta et al.*, 2002; *Liu et al.*, 2011]. However, this effect has not been quantified [e.g., *Cecil and Zipser*, 2002], as it depends on mixed-phase cloud processes, which are not well known [*Rosenfeld and Woodley*, 2000] and related to specific properties of the supercooled water and the ice content of each storm cloud. Several studies show that ice-scattering channels at relatively lower frequencies, such as the 37 and 85 GHz channels used in this work, are more sensitive to emissions by liquid water than the higher-frequency channels such as 150 GHz [e.g., *Spencer et al.*, 1983], which is also studied in the present investigation. Moreover, the 150 GHz channel is only moderately affected by variation in the ground emissivity, while the water vapor channels (near 183.3 GHz) are generally insensitive to lower precipitation [*Bennartz and Bauer*, 2003].

Numerous works have highlighted the significance of radiometric signatures at water vapor channels near the 183.3 GHz absorption line, i.e., 183.3 ± 1, 183.3 ± 3, and 183.3 ± 7 GHz, to study convective systems [e.g., *Burns et al.*, 1997; *Wang et al.*, 1997; *Staelin and Chen*, 2000; *Bennartz and Bauer*, 2003; *Hong et al.*, 2005; *Leppert and Cecil*, 2015]. In the presence of storm-associated scattering media, typically having a large amount of sizable ice particles (e.g., 0.2 g/m^3) below a small amount of water vapor and ice crystals, the Tbs for these channels are significantly depressed. For example, 183.3 ± 7 GHz can be depressed by more than 100 K due to water vapor absorption within the cloud and hydrometeor scattering, and there is no sensitivity to ground emissions [e.g., *Burns et al.*, 1997; *Wang et al.*, 1997]. Importantly, simulation studies have indicated that for a given altitude these channels are much more sensitive to changes in the ice content than the liquid water content, since ice particles present higher scattering coefficients than liquid hydrometeors [e.g., *Muller et al.*, 1994; *Bennartz and Bauer*, 2003]. For example, at low altitudes such as 4–6 km, the 89 GHz channel is sensitive to presence of liquid water (up to 10 K), whereas 183.3 ± 3 GHz is mostly insensitive to it [*Bennartz and Bauer*, 2003]. Consequently, the water vapor channels provide a set of Tb measurements that are less affected by liquid water than other ice-scattering channels.
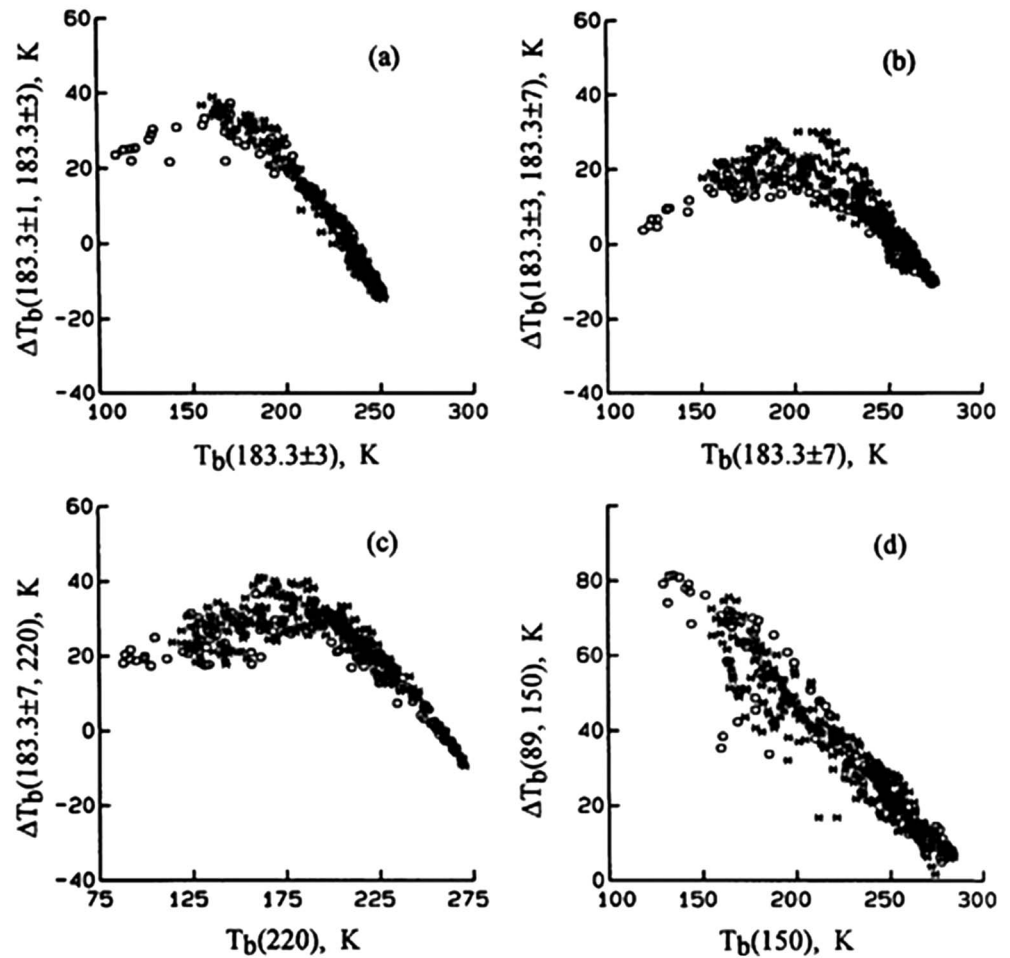
Figure 1. Reproduction of *Wang et al.* [1997, Figure 11]. The scatterplot of ΔTbs and Tbs from pairs of microwave channels on an airborne radiometer for two storms. (a) ΔTb13 versus 183.3 ± 3 GHz, (b) ΔTb37 versus 183.3 ± 7 GHz, (c) ΔTb (183.3 ± 7−220 GHz) versus 220 GHz, and (d) ΔTb(89−150 GHz) versus 150 GHz.

In addition to Tbs, differences in Tbs (ΔTbs) between the water vapor channels are also pivotal to the understanding of convective systems. Each channel senses different depths in the cloud since their correspondent weighting functions maximize at different altitudes, as reported by *Burns et al.* [1997]. According to *Hong et al.* [2005], the 183.3 ± 7 GHz channel senses deeper regions of the storm cloud and is the most responsive to ice particles, whereas 183.3 ± 1 and ±3 GHz channels are typically insensitive to snow. In general, the farther the frequency is from the center of the water vapor line (183.3 GHz), the larger the correspondent Tb depression due to ice particles. *Burns et al.* [1997], using simulated and measured Tbs of a storm system, proposed a criterion based on the difference between measured brightness temperatures at 183.3 ± 3 and 183.3 ± 1 GHz to screen out convective clouds before water vapor retrieval.

Subsequent studies applied the method described in *Burns et al.* [1997] to examine convective systems (instead of removing them as noise). For example, *Wang et al.* [1997] used the water vapor channels, along with 89, 150, and 220 GHz, to study deep convection and assess the properties of frozen hydrometeors. Their investigation employed two airborne microwave radiometers and observed two different storms. Their results were compared to simulated outputs of hydrometeor, temperature, and relative humidity profiles. These simulated outputs were also used to generate radar reflectivity calculations from hydrometeor profiles through a general cloud ensemble model, the University of Wisconsin version of the Regional

Atmospheric Modeling System (RAMS). The RAMS results were applied to a radiative transfer model that incorporates Eddington's second approximation [e.g., *Wu and Weinman*, 1984] to calculate the modeled Tbs at the top of the atmosphere for all the frequency channels available from their sensor, a millimeter-wave imaging radiometer. One of main conclusions of Wang et al. is that the modeled Tbs at 89, 150, and 220 GHz are less responsive to parameters (such as the size distribution of hydrometeors) when compared to the measured Tbs. This discrepancy between modeled and measured values did not occur with the three water vapor channels. Wang et al. showed that as the amount of ice hydrometeors becomes increasingly larger, the ice-scattering signature became more prevalent and the Tbs decrease. Moreover, Wang et al. (their Figure 11 is shown as our Figure 1) found that for regions of deep convection there is a positive correlation between any high-frequency Tb (89, 150, 200, and three 183.3 GHz channels) and differences between the water vapor channels, which will be referred in this paper as ΔT_{17} (Tb at $183.3 \pm 1 -$ Tb at 183.3 ± 7), ΔT_{13} (Tb at $183.3 \pm 1 -$ Tb at 183.3 ± 3), and ΔT_{37} (Tb at $183.3 \pm 3 -$ Tb at 183.3 ± 7).

Hong et al. [2005, Figure 1], using Advanced Microwave Sounding Unit (AMSU)-B observations, confirmed the results of *Wang et al.* [1997] and found a positive correlation between Tbs and ΔTbs when the Tb depressions were large (deep convection). However, Figures 1a–1c (Figures 11a–11c in Wang et al.) show that for weaker convection there is a negative correlation (negative slope) between Tbs of ice-scattering channels and ΔT_{17}, ΔT_{13}, and ΔT_{37}. This is similar to the relationship shown in Figure 1d (Figure 11d in Wang et al.) where the ΔTb is the difference of 89 and 150 GHz rather than a pair water vapor channels like Figures 1a–1c. In situations where the convection is stronger, the amount of water vapor in regions above the ice hydrometeors becomes increasingly smaller, and the water vapor channels simply act as ice-scattering channels. In this case, the slope in ΔTb versus Tb plots is positive as shown in Figures 1a–1c. If Tbs are below around 170 K, then ΔT_{17}, ΔT_{13}, and ΔT_{37} are approximately constant since the amount of water vapor above the ice layer is approximately zero. In agreement with these results from Wang et al., *Hong et al.* [2005] using AMSU-B data and *Hong and Heygster* [2008] using SSMIS data established the following criteria for identifying intense tropical convection:

$$\Delta T_{17} \; > \; \Delta T_{13} \; > \; 0 \; K, \Delta T_{17} \; > \; \Delta T_{37} \; > \; 0 \; K, \tag{1}$$

and

$$T_f \leq T_{c,f}, \tag{2}$$

where T_f is the Tb at the frequency f and $T_{c,f}$ is the empirical threshold temperature. When AMSU-B data are used, as in *Hong et al.* [2005], $T_{c,f}$ is a function of the viewing angle because the variations of the AMSU-B viewing angles have an impact on the Tb measurements. When data are from SSMIS, as in *Hong and Heygster* [2008], $T_{c,f}$ is the Tb threshold that was determined by *Zipser et al.* [2006]. According to *Hong and Heygster* [2008], the Tb threshold for the 1% most intense convective clouds is $T_{c,f} = 166.1$ K for the 183.3 ± 1 GHz channel. We note that these criteria in equations (1) and (2) agree directly with results of *Wang et al.* [1997] and identify the positive slope and flat regions of the plots in Figure 1 where deep convection is identified.

We now proceed to review connections between lightning, Tbs, and hydrometeors. Many prior investigations have analyzed lightning occurrence in conjunction with passive microwave Tbs. Commonly used frequency channels reported in past studies are: 37 GHz [e.g., *Zipser et al.*, 2006; *Cecil*, 2009; *Liu et al.*, 2011], 85–91.7 GHz [*Schols et al.*, 1999; *Toracinta and Zipser*, 2001; *Boccippio et al.*, 2000; *Nesbitt et al.*, 2000; *Zipser et al.*, 2006; *Cecil et al.*, 2002, 2005; *Kodama et al.*, 2007; *Nakamura et al.*, 2011; *Liu et al.*, 2011], and 150–157 GHz [*Hong and Heygster*, 2008; *Nakamura et al.*, 2011], all of which are modulated by the ice layer. *Peterson et al.* [2015] developed a method that further connects passive microwaves Tbs at 37 and 85 GHz with cloud electric fields, showing that such fields can be directly estimated from Tbs. All of these works have suggested that lightning flash rates and probabilities are connected with Tb depressions, supporting mechanisms that link deep convection and atmospheric discharges. Other important channels for lightning-related investigations, but not as commonly used, are the water vapor frequencies 183.3 ± 1, 3, and 7 GHz, which, as previously explained, are intense convection trackers. *Hong and Heygster* [2008] applied equation (1) to SSMIS data to pinpoint tropical (30°S–30°N) deep convection. They studied the geographical distribution of the most intense convective storms for 1 year of data, showing that such systems were mainly concentrated over central and South America, tropical western Africa, and northern Australia. These results were compared to lightning measurements from the Lightning Imager Sensor (LIS) for the same period, in terms of mean flash rates per hour in 0.1° × 0.1° boxes. They found that, in general, the geographical distribution of intense convective systems as defined by their criterion is in agreement with the distribution of LIS flashes. According to

Hong and Heygster [2008], lightning occurrence geographically matches intense convective systems and the use of water vapor channels is important not only for pinpointing deep convective systems, but also for analyzing those systems in terms of lightning incidence. However, Hong and Heygster did not use a temporally coincident lightning/Tb database, which is what we do in the present investigation.

Robust connections between lightning and cloud ice-related parameters indicate that the noninductive mechanism plays a major role in cloud electrification, dominating the electric field growth and subsequent lightning production in all seasons, on a global scale, for oceanic and land-based thunderstorms [e.g., *Latham et al.*, 2007]. This mechanism involves ice-ice collisional charging, is independent of external electric fields [e.g., *Jayaratne et al.*, 1983; *Takahashi*, 1984], and relies on vigorous updrafts in the mixed-phase region [e.g., *Reynolds et al.*, 1957; *Lang and Rutledge*, 2002; *Wiens et al.*, 2005; *Deierling and Petersen*, 2008], as well as the presence of supercooled water at heights with temperatures between 0°C and −10°C [e.g., *Schols et al.*, 1999]. The inductive mechanism, another process of cloud charging, is described as a nondominant process that, similar to the noninductive mechanism, depends on hydrometeor collisions but requires external electric fields [e.g., *Mansell et al.*, 2005]. Inductive charging might play a significant role in the final stages of field growth, but the efficacy of this mechanism is reduced as the ice content increases in the mixed-phase region [e.g., *Petersen et al.*, 2005; *Latham et al.*, 2007]. Conversely, the noninductive mechanism relies on ice production rate. Thus, positive correlations between lightning rates and cloud ice concentration, and therefore Tb depressions, indicate the importance of the well-established noninductive mechanism rather than the inductive mechanism.

The lightning measurements used in this investigation are provided by WWLLN. WWLLN is a developing, global lightning detection network that has been increasingly used for a diverse set of applications in atmospheric electricity studies. For example, WWLLN has been used to quantify the connections between hurricane intensity change and lightning occurrence [*Price et al.*, 2009] and to examine the polarity and energetics of lightning within the inner core regions of North Atlantic hurricanes [*Thomas et al.*, 2010]. WWLLN continually detects the strongest strokes that are, for the vast majority, CG discharges [*Rudlosky and Shea*, 2013]. The detection efficiency of WWLLN has been quantified [e.g., *Hutchins et al.*, 2012a], and this is a relevant topic of discussion in section 2.

2. Data and Methods

The WWLLN (approximately 60 stations worldwide during 2009–2011; http://wwlln.net) provides real-time lightning locations globally by measuring the time of group arrival of very low frequency (VLF) electromagnetic radiation (3–30 kHz) generated by lightning strokes [*Dowden et al.*, 2002; *Rodger et al.*, 2006; *Virts et al.*, 2013]. The location accuracy and efficiency of WWLLN have been determined by comparison to regional and ground-based, lightning detection systems [*Lay et al.*, 2004; *Rodger et al.*, 2005, 2006, 2009; *Jacobson et al.*, 2006; *Abarca et al.*, 2010] and LIS on the TRMM satellite [*Rudlosky and Shea*, 2013]. *Rodger et al.* [2009] used a comparison between WWLLN and the New Zealand Lightning Detection Network and Monte Carlo simulation techniques to estimate the global location accuracy of WWLLN. *Abarca et al.* [2010] conducted a performance assessment of WWLLN using the National Lightning Detection Network (NLDN) as ground truth over the contiguous U.S. In these studies, the overall detection efficiency of cloud-to-ground strokes increased from about 4% in 2006–2007 to about 11% in 2008–2009 (>30% for strokes with peak currents > 35 kA), and location and timing errors were less than 10 km and 10 μs, respectively. In a comparison of WWLLN and LIS on the TRMM satellite, *Rudlosky and Shea* [2013] found that in the broad tropics (between 38°N and 38°S) of the Western Hemisphere the total WWLLN detection efficiency of LIS flashes steadily improved from 6% in 2009 to 9.2% in 2012 with a mean location difference of 11 km. They also found that WWLLN tended to detect the strongest LIS flashes that were more likely to be CG flashes. Thus, WWLLN detects both CG and intracloud (IC) lightning, but since it is biased toward lightning that radiates strongly in the VLF, it detects CG strokes more efficiently than IC lightning.

Quantifying the detection efficiency of WWLLN is important for comparing lightning with radiometer data. *Hutchins et al.* [2012a] developed a technique to generate near real-time, global relative detection efficiency (DE) maps for WWLLN with a temporal resolution of 1 h and spatial resolution of 1° × 1°. The relative DE corrections account for changes in the ionosphere and the operational status of stations and thus allows for adjustment of the measured lightning density as though WWLLN had uniform global detection efficiency.

Table 1. Satellite Microwave Radiometer Data

Platform	Orbit	Instrument	Scanning Geometry	Frequencies (GHz) and Polarization	Resolution or Effective Field of View (km)	Swath Width (km)	Operational Period	Reference
TRMM	35°/400 km	TMI	Conical	37 V/H, 85 V/H	7 × 5 at 85 GHz, 16 × 9 at 37 GHz	759	1997–2015	Kummerow et al. [1998]
DMSP/F16	Polar/830 km	SSMIS	Conical	91.7 V/H, 150 H, 183.3 ± 1, 3, 7 H	12.5 × 12.5	1707	2003–up to present	Yan and Weng [2009]

In other words, this technique compensates for the uneven global coverage of network sensors, as well as variation in VLF propagation. Importantly, although WWLLN is a ground-based network, there is not a significant land/ocean difference in its detection efficiency [*Hutchins et al.*, 2012a, 2012b]. This is due to the enhanced VLF propagation over the ocean and the large number of WWLLN receivers across most of the continents.

Relative DE corrections can be applied to all archived WWLLN data recorded since April 2009. *Hutchins et al.* [2012a, Figures 14–16] compared the raw versus relative DE-corrected WWLLN global stroke density for 2011, and they found that the region most affected by applying relative DE corrections is central Africa due to sparse WWLLN coverage. In parts of central Africa, the stroke density increases by 1 to 10 strokes/km^2/yr after applying the relative DE corrections. Figures S1 and S2 in the supporting information are DE and non-DE-corrected WWLLN lightning density maps for locations and times coincident with SSMIS and TMI for the combined summers of 2009-2011. In Figures S1 and S2, we also find that the region with some of the greatest DE corrections is central Africa. As explained in *Hutchins et al.* [2012b], Africa has a lower DE because of the small number of stations on the continent. More distant stations only detect stronger strokes because of the stronger attenuation of VLF propagation over land compared with over water. Figures S3 and S4 in the supporting information show that the lightning/Tb scatterplots of non-DE-corrected data and DE-corrected data are similar (see section 3 for details).

It is important to note that relative DE corrections only provide a multiplier (>1) to existing detected lightning rates. If WWLLN detects no lightning, then the relative DE corrections have no effect: no strokes are counted. This means that the calculations of the probability of at least one WWLLN lightning stroke are independent of DE corrections. Thus, our global comparison of WWLLN to radiometer data for the broad tropics is mostly insensitive to applying relative DE corrections. Finally, we note that our results using WWLLN data from 2009 to 2011 are generally representative of the network as of 2016, because there have been no major upgrades, other than a steady increase in detection efficiency by 50% or more since 2009 [*Holzworth et al.*, 2015].

The radiometric database used in this study combines TMI and SSMIS/F16 measurements of Tbs. These are Level 1C data from Colorado State University (http://rain.atmos.colostate.edu/). Table 1 summarizes the characteristics of the TMI and SSMIS microwave channels we use. In addition to these channels, polarization corrected temperatures (PCT), a weighted difference of vertical and horizontal polarizations to minimize surface emissivity effects from land and ocean, are found for TMI 37 and 85 GHz, and SSMIS 91.7 GHz channels [e.g., *Nesbitt and Zipser*, 2003]. TMI and SSMIS have some notable similarities and differences. First, both have conical scan geometries that provide uniform spatial resolution, polarization purity, and common concentric fields for all instrument channels across their swaths [*Kummerow et al.*, 1998; *Yan and Weng*, 2009]. Moreover, both instruments are on low-Earth orbiting (LEO) satellites allowing a particular region of Earth to be observed for only a few minutes each day. Although both are on LEO satellites, their actual orbits are quite different. The polar-orbiting DMSP satellites are in circular Sun-synchronous low orbits (830 km altitude), and they cross the equator at the same local solar time (LST) twice each day, once ascending (north to south) and once descending. Specifically, during the years studied here (2009–2011), DMSP/F16 crossed the equator at about 19:00 LST ascending and 07:00 LST descending with a period of 101 min or ~14 orbits daily (orbit degradation causes slow changes in these values over time). In contrast, the TRMM orbit is circular, non-Sun synchronous, and at an inclination of 35° (~400 km altitude) with a period of about 90 min (~16 orbits daily) that allows this satellite to observe surface locations at different daily local times and provide extensive coverage of the tropics. The main implication of these orbital differences is that
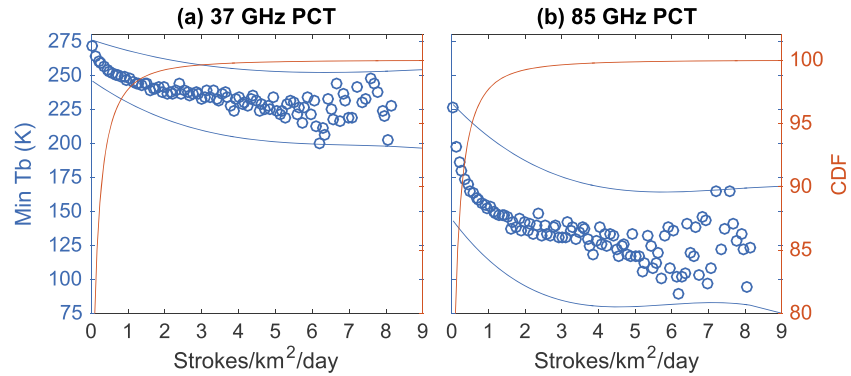
Figure 2. Scatterplot of TMI (a) 37 and (b) 85 GHz PCT brightness temperatures (Tbs) and WWLLN stroke rates for during warm seasons of 2009–2010 in the Northern Hemisphere (JAS) and 2010–2011 in the Southern Hemisphere (JFM). Lightning counts and minimum Tbs are found in 0.5° × 0.5° squares. Lightning occurred within ± 15 min of the Tb observations. Blue circles are the averages of the minimum Tb within the lightning bins, and the blue curves show the ± 1 standard deviation envelope of the Tbs. Cumulative distribution functions (CDFs) of the stroke rates are shown on the right ordinate in red.

SSMIS/F16 tends to observe thunderstorms that occur at about 19:00 and 07:00 LST, whereas TMI observes thunderstorms at various LSTs.

The TMI and SSMIS/F16 radiometers provide Tbs with resolutions and swath widths as indicated in Table 1. We parse these data by taking the minimum Tbs in 0.5° × 0.5° grid squares for the TMI and SSMIS/F16 frequency channels listed in Table 1 and the corresponding calculated PCTs. WWLLN data are parsed in the same 0.5° × 0.5° grid squares by counting the number of relative DE-corrected lightning strokes within ± 15 min of the Tb measurements. In total, the data set includes WWLLN lightning strokes coincident with Tb measurements and all Tbs with and without coincident strokes. WWLLN strokes that do not correspond spatially and temporally with the satellite Tbs, such as strokes outside of the radiometer swaths, are not included. We define a *gridded sample* as the collection of data comprising the ± 15 min lightning count (which can be 0) and the minimum Tbs for all channels (with the corresponding PCTs for 37, 85, and 91.7 GHz) for each 0.5° × 0.5° square scanned by TMI or SSMIS/F16. Gridded data for two Northern Hemisphere and Southern Hemisphere summers are combined into a summer database, namely July-August-September (JAS) of 2009 and 2010 for 0°–35°N and January-February-March (JFM) of 2010 and 2011 for 0°–35°S. These data are then organized into ocean, coast, and land domains using 0.5° × 0.5° resolution where the coast region is defined as within ±1° lat/lon of the coastline. We also convert lightning rates to units of strokes/km²/d. In total, this analysis includes approximately 5.8 million WWLLN strokes coincident with satellite radiometer observations from TMI and SSMIS/F16.
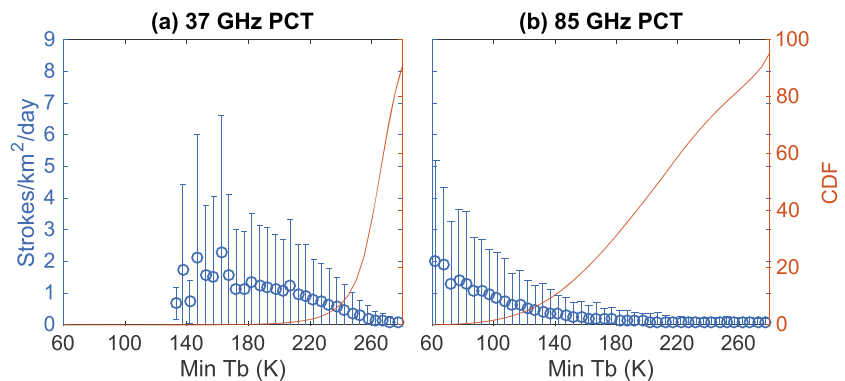
Figure 3. Scatterplot of TMI (a) 37 and (b) 85 GHz PCT brightness temperatures (Tbs) and WWLLN stroke rates. Similar to Figure 2 except that here blue circles are the averages of stroke rates within the Tb bins, and the error bars are the standard deviations of the stroke rates. Cumulative distribution functions (CDFs) of Tbs are shown on the right ordinate in red.
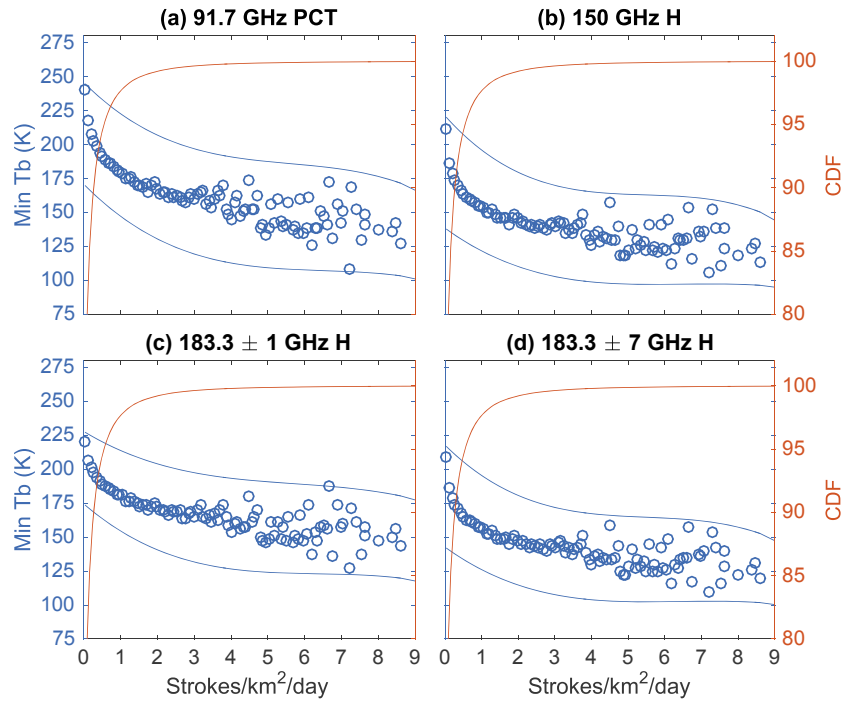
Figure 4. Same as Figure 2 except using SSMIS/F16 (a) 91.7 GHz PCT, (b) 150, (c) 183.3 ± 1, and (d) 183.3 ± 7 GHz H and WWLLN lightning rates.
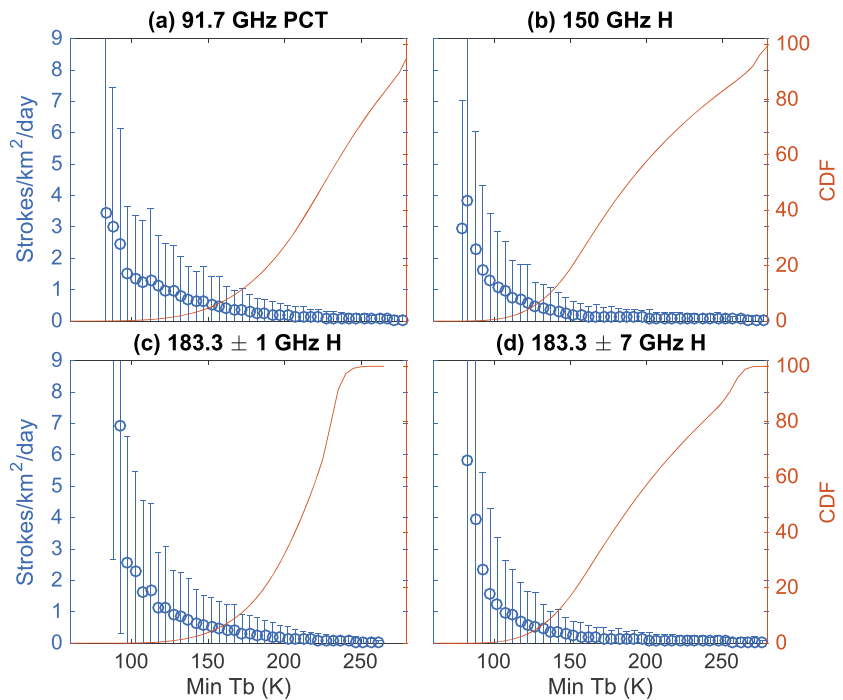
Figure 5. Same as Figure 3 except using SSMIS/F16 (a) 91.7 GHz PCT, (b) 150, (c) 183.3 ± 1, and (d) 183.3 ± 7 GHz H and WWLLN lightning rates.
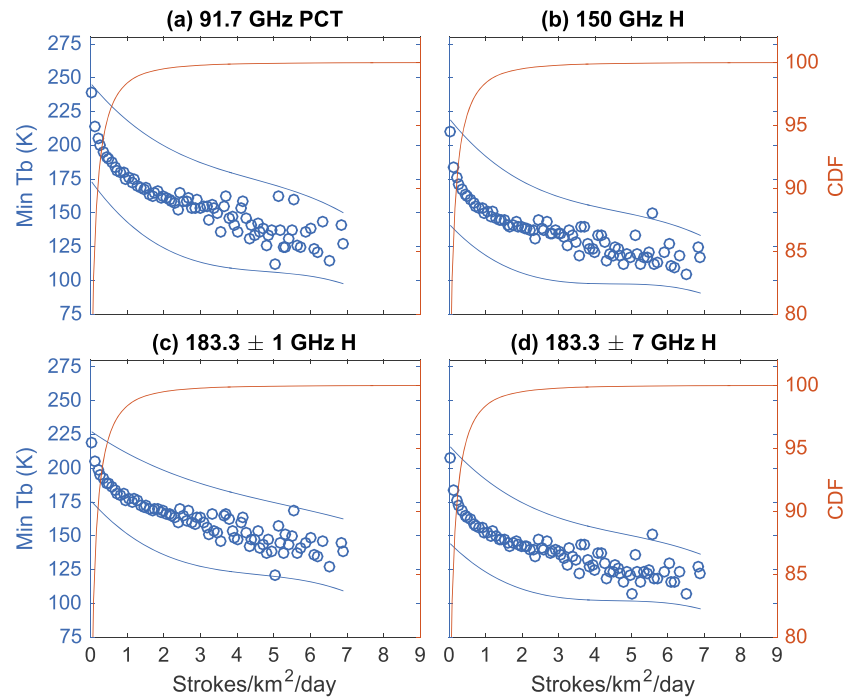
Figure 6. Same Figure 4 except using non-DE-corrected WWLLN stroke data.

3. Stroke Rate and Minimum Tb Scatterplots

The analysis shown in the scatterplots in Figures 2 through 6 is intended to display the overall relationship between stroke rates and individual TMI and SSMIS radiometer channels. Data presented in these scatterplots require additional processing using the gridded data described above as input. In Figures 2, 4, and 6, gridded data are redistributed by stroke rate in lightning bins with a width of 5 strokes per ±15 min per 0.5°×0.5° (or 0.08 strokes/km^2/d). To remove statistical outliers, only lightning bins with at least five gridded samples are included. Blue circles represent the average of minimum Tbs within a lightning bin, and blue curves show the ±1 standard deviation envelope of the Tbs. The cumulative distribution functions (CDFs) of stroke rates for each channel are presented on the right ordinates, in red. Figures 3 and 5 are also scatterplots, but here gridded data are redistributed by Tb in bins with a width of 5 K. Again, outliers are removed by including only Tb bins with at least five gridded samples. Blue circles represent the average of stroke rate within a Tb bin, and the error bars are the standard deviations of the stroke rates. The cumulative distribution functions (CDFs) of Tbs for each channel are presented on the right ordinates, in red. We note that Figures 2 through 5 use DE-corrected stroke data, whereas Figure 6 uses non-DE-corrected stroke data.

Previous studies [e.g., *Petersen et al.*, 2005; *Liu et al.*, 2011] indicated that increasing stroke rates are associated with decreasing Tbs for all the channels employed in our study. We point out that Liu et al. found that LIS flash rates have a stronger correlation with the areal extent of cold Tbs from TMI than minimum Tb. However, these authors determined that the correlations with minimum Tb are still robust (see section 7 for further discussion). Figures 2a and 3a present TMI 37 GHz PCT and stroke rates, showing a somewhat weaker trend compared to the other channels between minimum Tbs and lightning. This can be due to the reduced response of this channel to ice particles as reported by *Bennartz and Bauer* [2003] (for example) and increased response to lower precipitation. However, it must be noted that the 37 GHz channel has a smaller dynamic range than the higher frequencies; although the slope is less steep, the standard deviation is also smaller for 37 GHz. Also, in comparing Figures 2b and 3b (TMI 85 GHz PCT) and 4a and 5a (SSMIS 91.7 GHz PCT), the slope is steeper for the 85 GHz channel. As reported in previous results, TMI 85 and SSMIS 91.7 GHz present nonlinear physical differences, as well as different resolutions (see Table 1), and TRMM observes storms at various local solar times (LSTs) while DMSP/F16 observes at
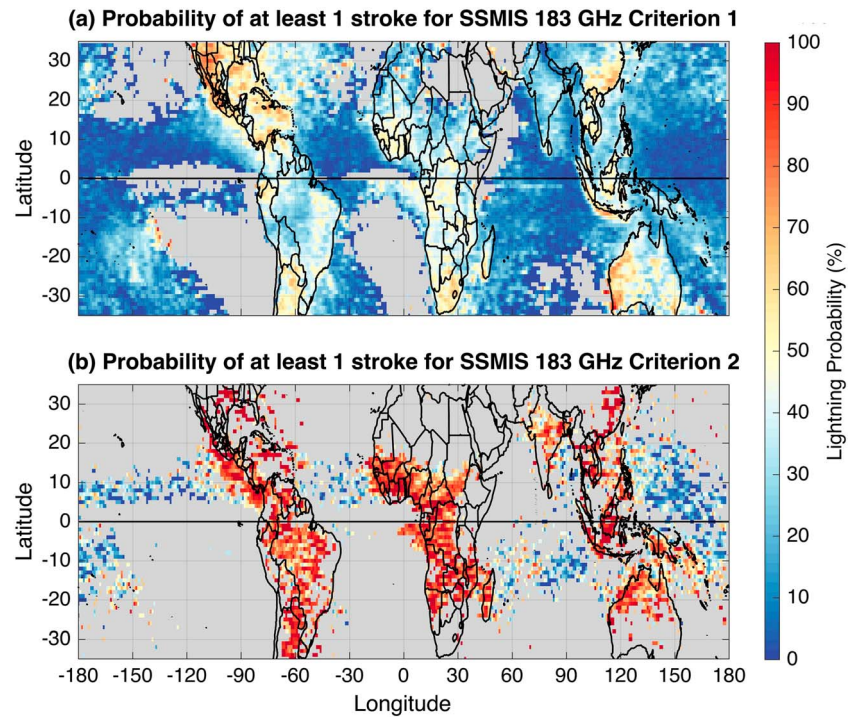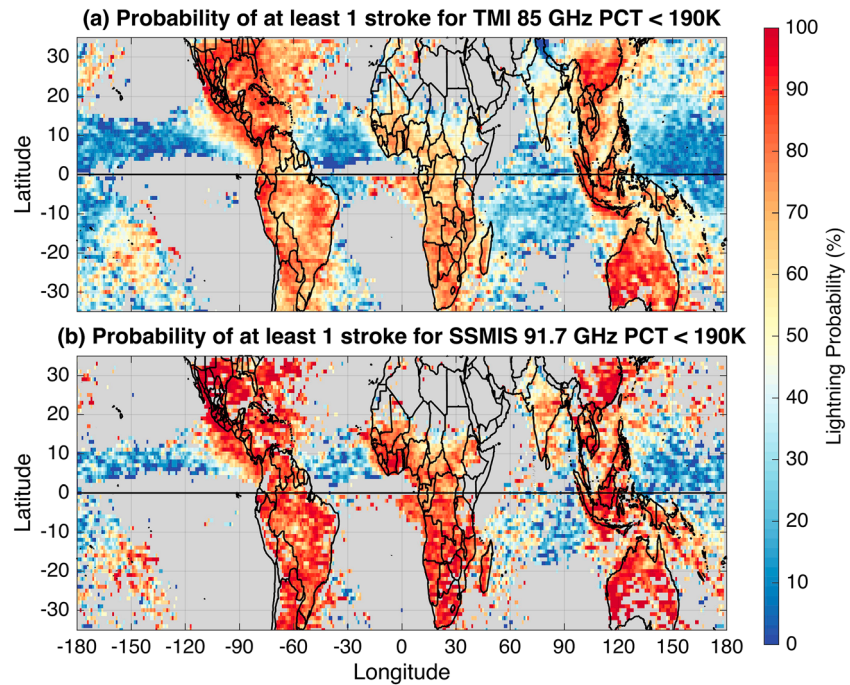
Figure 7. (a) Probability of at least one WWLLN lightning stroke given criterion 1 in *Hong and Heygster* [2008] for deep convection using SSMIS 183.3 GHz channels. (b) Probability of at least one WWLLN lightning stroke given criteria 1 and 2 in *Hong and Heygster* [2008] for deep convection using SSMIS 183.3 GHz channels.

fixed LSTs. For the three SSMIS water vapor channels (183.3 ± 1, ±3, and ±7 GHz), two of which are shown in Figures 4 and 5, the Tb depressions increase with channel width (183.3 ± 3 GHz is not shown but is intermediate in slope to 183.3 ± 1 and ±7 GHz). Moreover, the relationships between Tbs and stroke rates in Figures 4b and 5b (SSMIS 150 GHz H) and 4d and 5d (SSMIS 183.3 ± 7 GHz H) are remarkably similar. This is because the 183.3 ± 7 GHz channel can sense deeper into clouds than the other two water vapor channels [*Burns et al.*, 1997; *Hong et al.*, 2005] and, like the 150 GHz channel, is highly sensitive to frozen hydrometeors. These similar behaviors show that these two SSMIS channels deliver similar responses to intense convection.

Figure 6 shows the same data as Figure 4 for SSMIS channels, except that here non-DE-corrected WWLLN stroke rates are used. In comparing Figures 4 and 6, employing relative DE corrections has little effect on the scatterplots for stroke rates less than about 5 strokes/km^2/d. Stroke rates greater than 5 show some differences, notably the DE-corrected scatterplots extend to about 9 and the non-DE to about 7 strokes/km^2/d. For easier comparison of DE and non-DE data, Figures S3 and S4 in the supporting information are scatterplots of non-DE-corrected data overlaid on DE-corrected data for SSMIS and TMI coincident lightning. In general, the analysis is not particularly sensitive to employing relative DE corrections.

Figures 2 through 6 also include cumulative distribution functions (CDFs) of stroke rates and Tbs. For instance, Figures 2, 4, and 6 show that the top 1% of the CDF of stroke rates corresponds with about 2 strokes/km^2/d. Figures 3 and 5 show that the lowest few percent of the CDFs of Tbs corresponds with Tbs ranging from about 120–140 K for the 85/91.7, 150, and 183.3 GHz channels to about 230 K for the 37 GHz channel and also corresponds with stroke rates of about 1 stroke/km^2/d.

The scatterplot results provide evidence that a VLF ground-based network (WWLLN) can identify convective activity in association with microwave Tbs, including higher-frequency channels such as 150 and 183.3 GHz. Thus, our findings confirm and extend the conclusions of previous works [e.g., *Petersen et al.*, 2005; *Liu et al.*, 2011]. In section 6, we use these scatterplot relationships to reconstruct Tbs from stroke rates for a case study over Mexico.
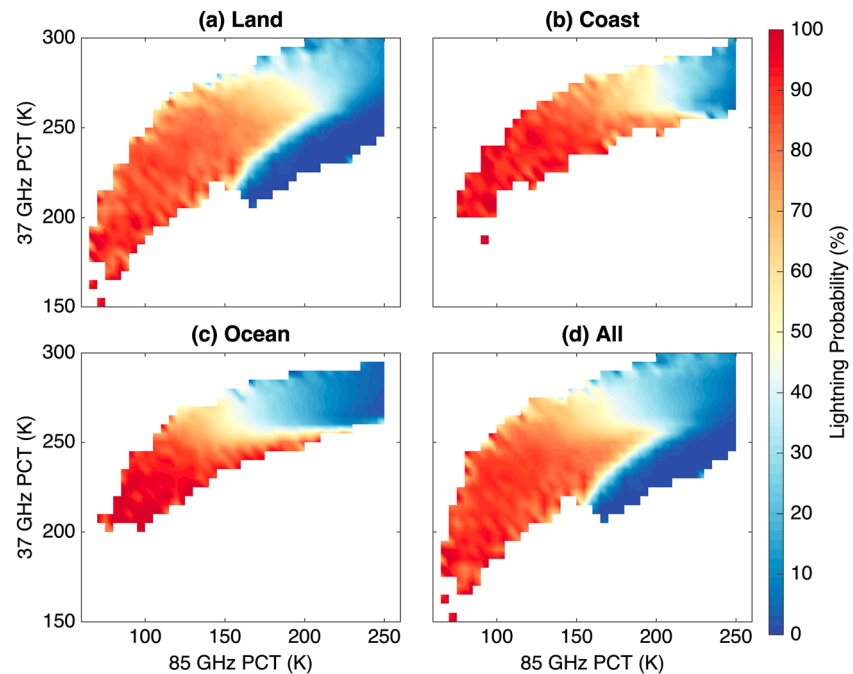
Figure 8. (a) Probability of at least one lightning stroke given TMI 85 GHz PCT below 190 K. (b) Probability of at least one lightning stroke given SSMIS 91.7 GHz PCT below 190 K.

4. Lightning Probability Maps

One of the prime objectives of this study is to determine the probability of lightning strokes in regions where intense convection was detected. First, we apply the gridded-samples parsing technique detailed in section 2 and the methods described by *Hong and Heygster* [2008] (see equations (1) and (2)) to identify deep convection over the periods of interest. We then quantify the probability of at least 1 stroke in the gridded sample. Figure 7a shows a map of probabilities of at least 1 stroke after applying the 183.3 GHz SSMIS channel criteria (all conditions) in equation (1) (from *Hong and Heygster* [2008]). High probabilities are found over some land regions including Central America, northern Argentina, coastal Australasia, southern China, southern United States, and Mexico, and low probabilities are found over oceans, as previously observed, for example, by *Liu et al*. [2011]. Figure 7a agrees with previous studies that linked intense convection and lightning occurrence, such as *Cecil et al*. [2005], *Petersen et al*. [2005], *Zipser et al*. [2006], and *Liu et al*. [2011]. These authors used different techniques associating Tbs or ice content parameters and lightning, with frequencies up to 85 GHz, and different types of restrictions for convection intensities. These previous results indicate that the technique that we applied to generate Figure 7a is robust regarding the detection of vigorous convection. However, it should be emphasized that the purpose of the figure is to locate where intense convection is associated with lightning, but not necessarily the most intense convective systems. As a result, the most common probabilities of strokes lie in the range between 0 and 25%. These probabilities, as expected, are commonly observed over the oceans. Figures S5 and S6 in the supporting information display the sample sizes (the numbers of gridded samples fitting the previously described criteria for intense convection). The low lightning probabilities over the ocean are not frequently associated with low sample sizes.

In addition to Figure 7a, we produced other similar maps that show the probability of at least 1 stroke associated with SSMIS and TRMM Tbs below a threshold temperature. One example is shown in Figure 8a, which displays the probability of one lightning stroke for TMI 85 GHz PCT below 190 K. This Tb threshold of 190 K was chosen since it is the approximate 85 GHz PCT value associated with the deepest 1% of convective systems in TRMM/TMI precipitating features [e.g., *Cecil et al*., 2005]. As the figure indicates, this criterion selects convective systems that are stronger and associated with more strokes than the systems displayed in Figure 7 a. As in Figure 7a, the maximum probability of strokes here is also 100%. The most common stroke probability

Figure 9. TMI 37 versus 85 GHz PCT and probabilities of at least one WWLLN lightning stroke.

range over the continents is 50–100%, whereas the typical probabilities over the oceans are between 0 and approximately 70%. These results indicate that convective systems over the oceans often have cold Tbs, but either do not produce lightning that is detected by WWLLN or have a lower probability of lightning when compared to systems over the land. We note that this is unlikely due to an efficiency issue of WWLLN, since the network does not have a land versus ocean detection efficiency bias [*Hutchins et al.*, 2012a, 2012b]. On the other hand, since the systems displayed in Figure 8a generally have colder Tbs than the ones shown in Figure 7a, such systems are generally associated with more lightning.

Figure 8b maps the probability of at least one lightning event given SSMIS 91.7 GHz PCT temperatures below 190 K. The results present differences, as well as similarities, from the map displayed in Figure 8a for TM 85 GHz PCT. The dissimilarities occur primarily because the satellite orbits are different and so are the sample sizes. The orbit of TRMM is restricted to ±35° of latitude, detecting systems within the broad tropics, whereas DMSP/F16 has a quasi-polar orbit. This difference means that, since we are studying the broad tropics, TRMM collects more data than SSMIS. Additionally, TRMM/TMI surveys one given area at different LST times of the day, whereas SSMIS passes over one given region twice a day at the same times every day (about 07:00 and 19:00 LST). According to, for example, *Zipser et al.* [2006] and *Liu and Zipser* [2008], the most intense continental convective systems are observed between 15:00 and 19:00 LST. Furthermore, over regions such as the Amazon basin and Central Africa, lightning occurrence has a late afternoon peak [*Virts et al.*, 2013]. These results imply that over land roughly half of the observations from SSMIS happen around the peak lightning activity. With a smaller sample size (Figures S7 and S8) and fixed local solar times of observation, the SSMIS 91.7 GHz PCT map presents approximately the same intense convection areas as the TMI 85 GHz PCT map (Figure 8a) but with greater probability of lightning occurrence.

The discrepancies between Figures 8a and 8b can also reflect inherent, nonlinear physical differences between 85 and 91.7 GHz ice scattering, such as reported by *Hawkins et al.* [2008], who compared SSMIS 91.7 GHz and Special Sensor Microwave/Imager (SSM/I) 85 GHz channels. Differences between the TMI and SSMIS sensors and platforms play an additional role. Although TMI 85 GHz has higher resolution than SSMIS 91.7 GHz (see Table 1), there is a significant limitation while using minimum 85 GHz PCTs from TMI, as described by *Bang and Zipser* [2015]. The TMI scan at this frequency has a data gap of approximately 7 km between scans, resulting in a significant probability of missing small areas of high ice content in a given continental storm. Such gaps mean that some results are misleadingly pairing unusually warm TMI 85 GHz
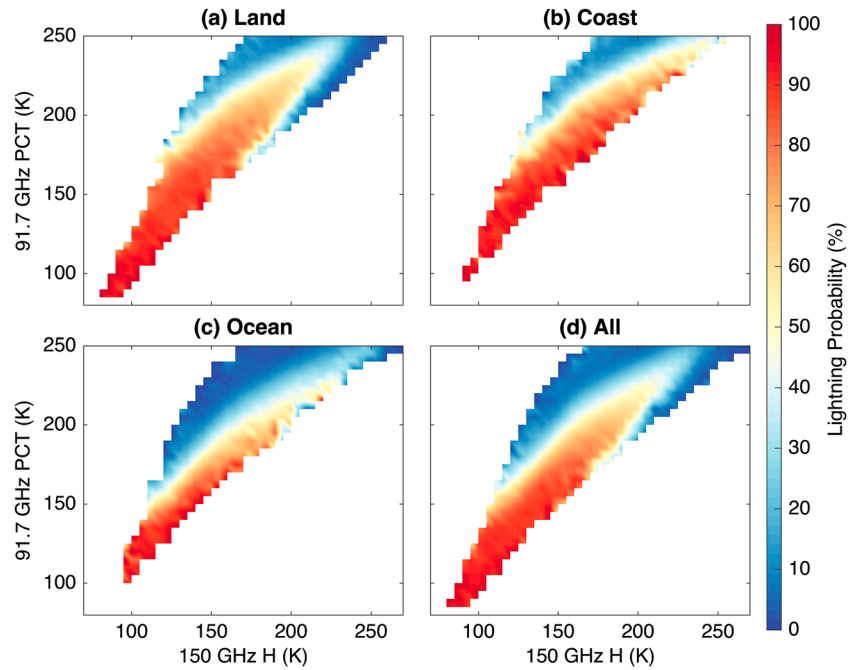
Figure 10. SSMIS 91.7 GHz PCT versus 150 GHz H and probabilities of at least one WWLLN lightning stroke.

Tbs with high lightning rates. This gap is not present in TMI 37 GHz and SSMIS high-frequency channels. Also, it should be noted that TMI and SSMIS have not been cross calibrated at these frequencies, although according to *Wimmers and Velden* [2007, Figure A1] the error between TMI and SSMIS at 85/91.7 GHz is less than about 8 K.
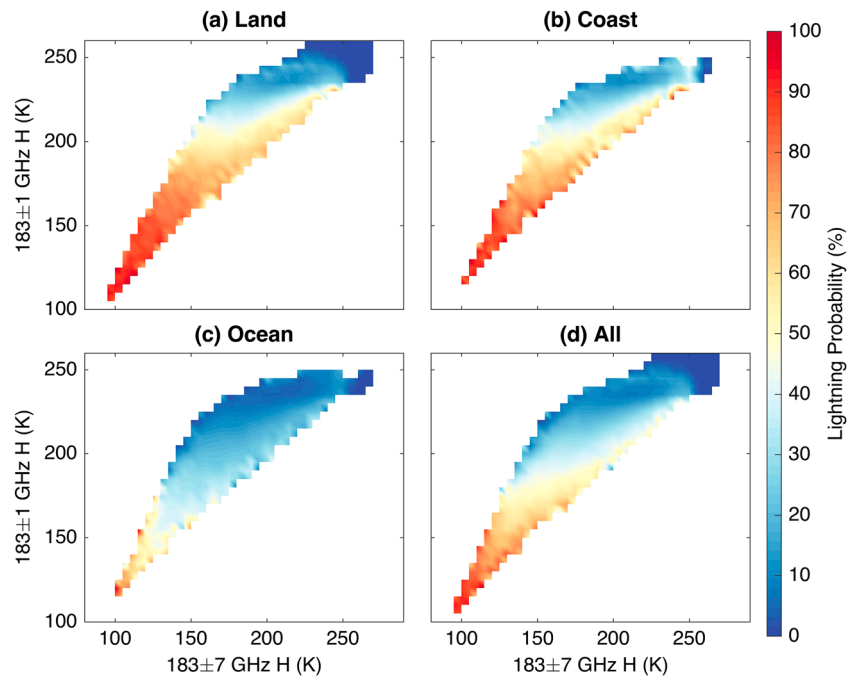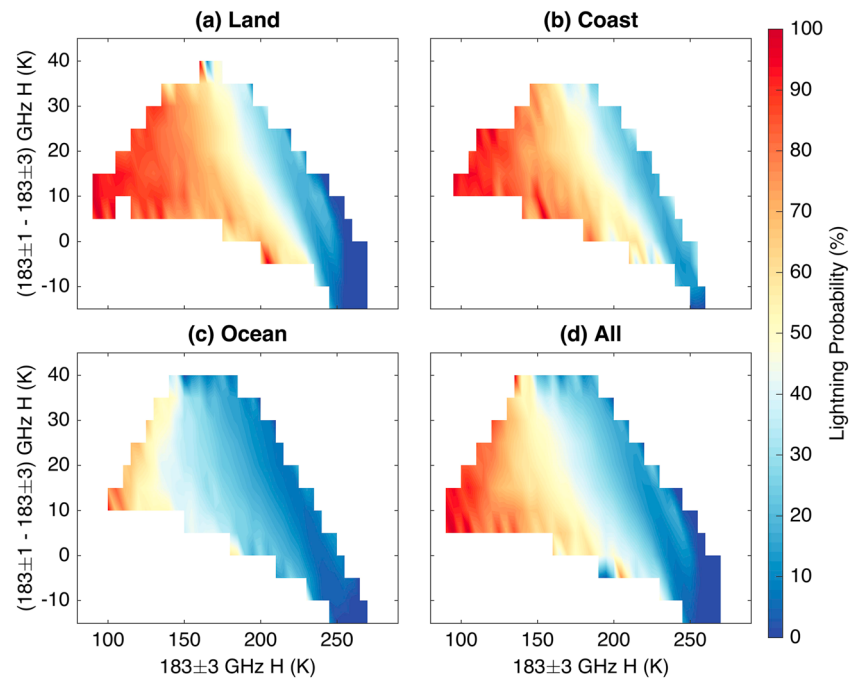

Figure 11. SSMIS 183.3 ± 1 GHz H versus 183.3 ± 7 GHz H and probabilities of at least one WWLLN lightning stroke.

Figure 12. SSMIS ΔTb_{13} versus 183.3 ± 3 GHz H and probabilities of at least one WWLLN lightning stroke. Compare with Figure 1a that shows results from *Wang et al.* [1997].

Figure 7b shows a map of the probabilities of at least one lightning stroke if equations (1) and (2) for SSMIS are applied. This method pinpoints the deepest 1% of convection as identified by *Hong and Heygster* [2008] with $T_{c,f} = 166.1$ K, however, with the additional analysis of the lightning (1 stroke) probability. Like in Figures 7a and 8, high probabilities are found over land and low probabilities over oceans. Unlike the results shown in Figures 7a and 8a, but similar to Figure 8b (although presenting a smaller sample size as shown in Figures S5 and S6), most land regions identified have a nearly uniform probability of 100%, indicating that the criteria used by Hong and Heygster select continental convective systems that are more likely to have at least one lightning stroke.

5. Dual-Frequency Analysis

Cecil et al. [2005], *Liu et al.* [2011], and *Nakamura et al.* [2011] are relevant references used in our investigation of lightning occurrence over land, ocean, and coastal areas and Tbs. These authors probed coincident measurements of discharges and cold Tbs in dual-frequency plots. While Cecil et al. and Liu et al. used TRMM precipitation features at 37 GHz and 85 GHz PCT to compare lightning rates and convection intensities, Nakamura et al. applied a similar concept to WWLLN lightning and AMSU-B measurements at 87 and 157 GHz in grid boxes of $0.5° \times 0.5°$. Figures 9 through 12 present similar analyses combining WWLLN stroke rates and Tbs from channels that range 37–150 GHz. We also probe Tbs from water vapor channels in an investigation similar to *Wang et al.* [1997], but now also using lightning stroke probabilities.

To study relationships between TRMM and SSMIS Tbs and lightning probabilities, we examine all the gridded samples over the period of study to determine the probability of at least one lightning stroke in dual-frequency plots. In Figure 9 we graph TRMM 37 versus 85 GHz Tbs and the probability of at least 1 stroke. The results are shown separately for land, coast, ocean, and, lastly, for all three regimes integrated. Because the presence of ice particles noticeably depresses Tbs at 37 and 85 GHz [e.g., *Wu and Weinman*, 1984], examining lightning probabilities in dual-frequency plots corresponds to comparing lightning rates with a vertically integrated ice water path weighted toward the larger frozen hydrometeors, although the presence of cloud water prevents the complete vertical characterization of the ice mass [e.g., *Vivekanandan et al.*, 1991]. This procedure is repeated for other pairs of SSMIS Tbs that are displayed in a similar fashion in Figures 10 through 12. In Figures 9 and 10, the cutoff Tb is 250 K for the TRMM 85 GHz PCT and SSMIS

91.7 GHz, respectively. This upper temperature limit was imposed so as to select convective systems, avoiding contamination by nonconvective, warmer clouds. In Figure 9, as in Figures 10 and 11, warmer Tbs are related to reduced lightning rates, and the highest lightning probabilities are mostly at the coldest Tbs, a result that is more evident for the oceanic regimes. In agreement with reports such as *Cecil et al.* [2005], *Liu et al.* [2011], and *Nakamura et al.* [2011], high lightning rates somewhat favor the right side of the population (toward higher 85 GHz PCT or 150 GHz Tbs, as shown in Figures 9 and 10), particularly over the ocean. Specifically, Figure 9c shows a seemingly anomalous region with 37 GHz PCT 240–250 K and 85 GHz PCT 150–210 K with surprisingly high probability of lightning. *Cecil et al.* [2005] speculated that this could be due to the transition from Rayleigh scattering to Mie scattering as hydrometeor sizes change or emissions from supercooled water or rainwater. Such effects would raise the higher-frequency (85 and 150 GHz) temperatures, enhancing conditions for cloud electrification. However, caution should be exercised while examining the 85 GHz PCT results, as there is the caveat of a 7 km gap between the TMI scans as reported by *Bang and Zipser* [2015]. This sensor can miss small, but electrically active, thunderstorms at 85 GHz. In totality, the results presented in Figures 9 through 12 show a positive, although nonlinear, trend between lightning probabilities and dual-frequency Tbs, indicating that highly convective clouds contain a significant amount of large-sized frozen hydrometeors. This result supports the noninductive mechanism of cloud electrification, in which lightning rates increase with increasing frozen hydrometeor mass (or Tb depressions). We also find that convective systems over the ocean can have cold Tbs that are not accompanied by lightning detected by WWLLN. Previous reports have indicated similar results [e.g., *Cecil et al.*, 2005; *Liu et al.*, 2011].

As in Figure 9, in Figure 10 we graph SSMIS 91.7 GHz PCT versus 150 GHz H Tbs and the probability of at least 1 stroke over land, coast, ocean and all regimes integrated. Again, we choose such frequencies for this dual-frequency plot to compare lightning probabilities with a vertically integrated ice water path weighted toward the larger frozen hydrometeors [e.g., *Nakamura et al.*, 2011]. As previously stated, the 150 GHz channel is only moderately affected by variation in the ground emissivity and is less affected by the liquid water content than channels with lower frequencies [e.g., *Bennartz and Bauer*, 2003].

In Figure 10, where the cutoff temperature is the same as in Figure 9 (250 K), the results are generally similar to the ones presented for Figure 9. Again, the previously discussed differences between the two sensors must be regarded in this analysis. In Figure 10 there is a more evident trend of higher lightning probabilities toward higher 150 GHz Tbs (when compared to the 91.7 GHz temperatures). This trend, as expected, does not corroborate Cecil et al.'s speculations when working with 85 GHz PCT, since the 150 GHz channel, unlike the 85 GHz PCT channel, has reduced sensitivity liquid water when compared to the sensitivity to the ice content. Our results indicate that warmer 150 GHz temperatures are, indeed, associated with a higher probability of lightning in all regimes, especially over the oceans. On the other hand, as in the previous results, there is a significant amount of cold convective systems without detected discharges over the oceans.

As in Figures 9 and 10, in Figure 11 we graph SSMIS 183.3 ± 1 GHz versus 183.3 ± 7 GHz Tbs and the probability of at least 1 stroke. As previously described, these water vapor channels act as ice-scattering channels while sensing convective systems. It is still possible to observe that, for coincident measurements of lightning probabilities and 183.3 GHz Tbs, the higher stroke probabilities tend to be located at warmer 183.3 ± 7 Tbs compared with the other 183.3 GHz channels. While the SSMIS 183.3 ± 7 channel senses similar types of hydrometeors as the 150 GHz channel, the 183.3 ± 1 GHz channel senses shallower regions in the ice layer, as described in section 1. The presence of cold Tbs without lightning over the ocean is now even more evident.

To further understand the relationship between intense convection and lightning occurrence, we apply a method similar to that used by *Wang et al.* [1997]. In Figure 12 we plot the probabilities of at least one lightning stroke for values of SSMIS 183.3 ± 1 GHz and ΔT_{13}. Here we see high lightning probabilities for 183.3 ± 1 GHz Tbs below about 200 K and ΔT_{13} values of about 5 to 25 K, with higher probabilities corresponding to lower values of 183.3 ± 1 GHz and ΔT_{13} over the land and coast. As discussed in section 1 and shown in Figure 1, Wang et al. identified deep convection (without lightning data) for similar ranges of SSMIS 183.3 ± 1 GHz and ΔT_{13} brightness temperatures and associated such values with ice scattering. We note that equation (1) from *Hong and Heygster* [2008] provides values of 183.3 ± 1 GHz and ΔT_{13} that obey the criteria Wang et al. used to identify deep convection. Thus, the results in Figure 12 agree
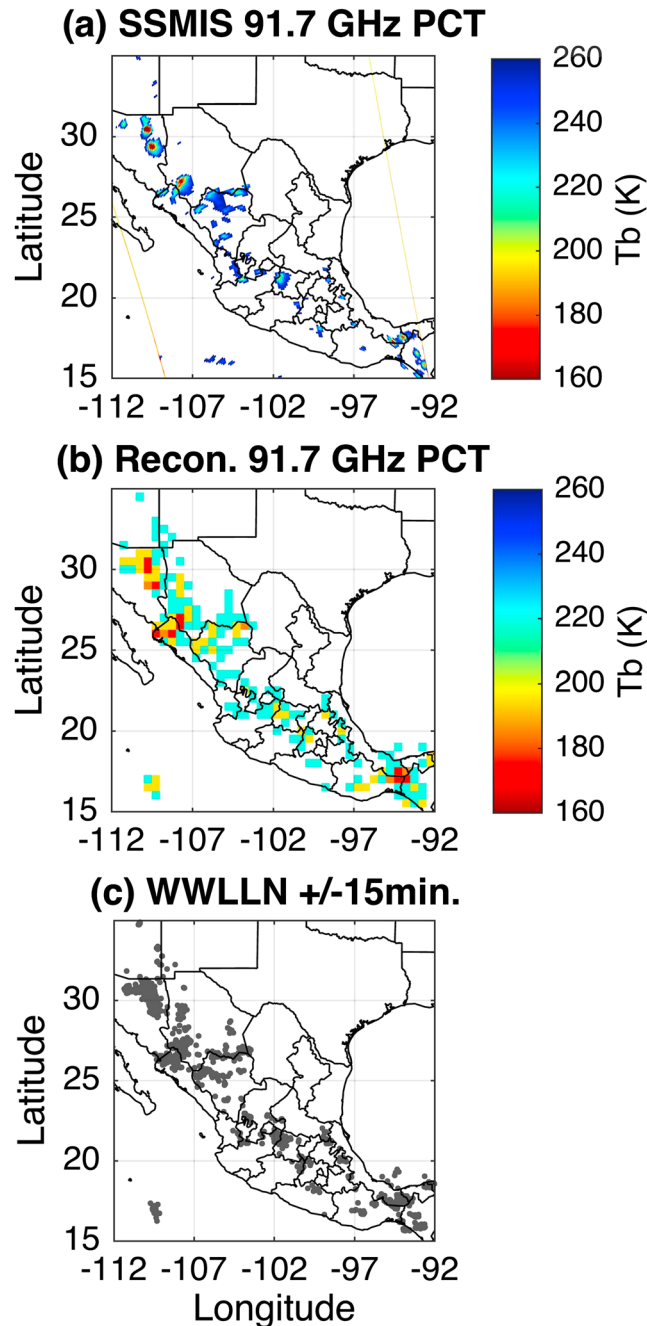
Figure 13. SSMIS-F16/WWLLN case study over Mexico at ~1900 LT, 14 August 2010. (a) SSMIS 91.7 GHz PCT data. (b) Reconstructed 91.7 GHz PCT data from WWLLN stroke rates and using scatterplots results in section 3. (c) Lightning strokes (gray dots) for ±15 min of SSMIS pass time.

with Figure 7, namely, where there is deep convection, we find high lightning stroke probabilities. As in Figures 9 through 11, the land/ocean differences are also noticeable, with much lower lightning stroke probabilities over the ocean.

Our analysis of lightning and radiometric dual frequencies complements previous dual-frequency studies that used LIS data [e.g., *Cecil et al.*, 2005; *Liu et al.*, 2011] with ground-based lightning data from WWLLN. Moreover, we show for the first time that the method of *Wang et al.* [1997] and *Hong and Heygster* [2008] to identify convection using the water vapor channels at 183.3 GHz also characterizes regions of high lightning probabilities.

6. Case Study

Our analysis thus far has included combined results for the entire broad tropics. In this section, we present results of a case study of a satellite pass and lightning data. Specifically, in Figures 13 through 15, we examine WWLLN data within ±15 min of a SSMIS pass over Mexico at ~1900 LT on 14 August 2010. Figure 13a shows the SSMIS 91.7 GHz PCT data, and Figure 13c shows the lightning strokes (gray dots). In agreement with our combined results, lightning strokes are located at or near regions where SSMIS measured Tb depressions. In Figure 13b, we take this comparison between lightning and Tbs a step further and reconstruct 91.7 GHz PCT data from WWLLN stroke rates. This is done by using a stepwise approximation to the scatterplot in Figure 6a. The reconstructed Tbs in Figure 13b agree with SSMIS measured Tbs in Figure 13a, which suggests that WWLLN lightning stroke rates can be used to fill in gaps in satellite data. In Figure S9 in the support-

ing information, we present a scatterplot of reconstructed Tbs versus measured Tbs for Figures 13a and 13b. The correlation coefficient for the mean of measured Tbs versus reconstructed Tbs is $r = 0.93$. This should be interpreted cautiously as there are only four data points used here (due to binning the Tbs) and $p = 0.07$. In addition to this example, we have found many other instances where stroke rates can be used to reconstruct Tbs for storms over land regions. However, in examining storms over the ocean such as tropical cyclones, we have found that stroke rates are less reliable at reconstructing Tbs [*Solorzano and Thomas*, 2015].

(a) SSMIS 150 GHz H

(b) SSMIS 183±1 GHz H
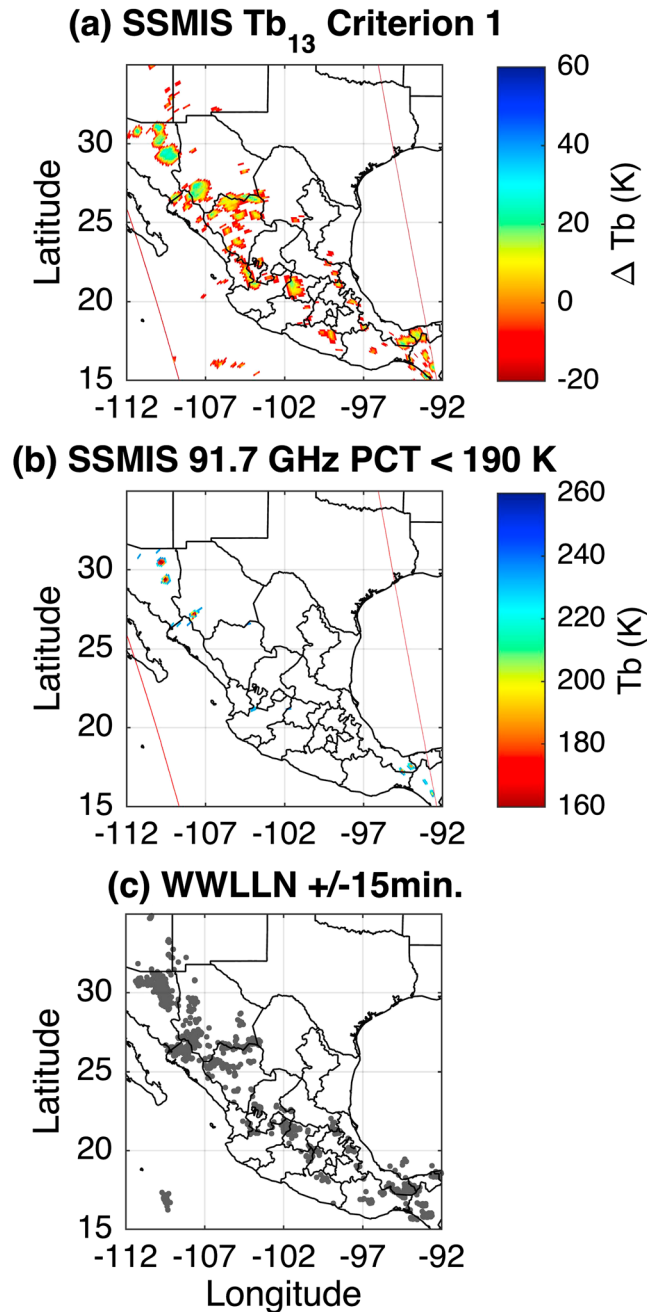

(c) WWLLN +/-15min.
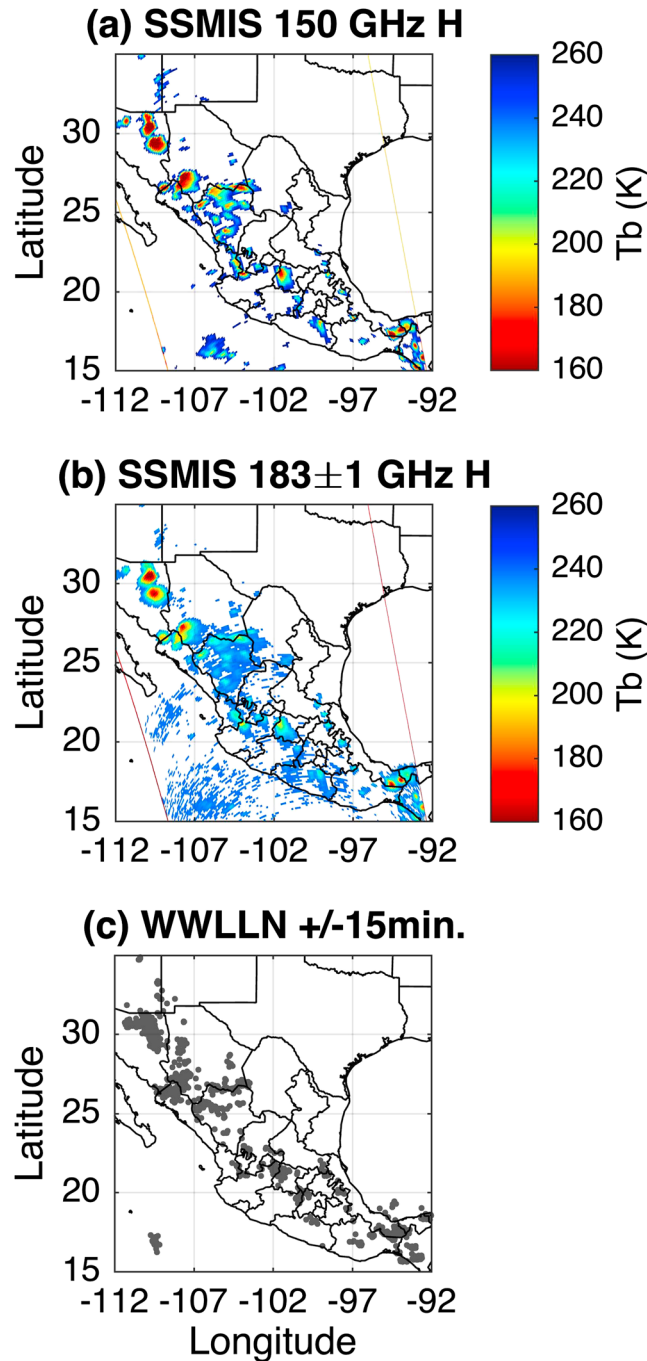
Figure 14. SSMIS-F16/WWLLN case study over Mexico at ~1900 LT, 14 August 2010. (a) SSMIS 150 GHz H data and (b) SSMIS 183.3 ± 1 GHz H data. (c) Lightning strokes (gray dots) for ±15 min of SSMIS pass time.

For the same SSMIS pass, Figure 14a shows SSMIS 150 GHz data, Figure 14b shows SSMIS 183.3 ± 1 GHz data, and Figure 14c shows WWLLN lightning data. Again, we find that stroke locations correspond with regions of Tb depressions. We note that the 183.3 ± 1 GHz channel in Figure 14b also detects faint Tb depressions due to water vapor in nonstorm regions. Figure 15a shows ΔT_{13} after applying criterion 1 in section 2 from *Hong and Heygster* [2008]. We find that stroke locations in Figure 15c correspond with regions identified as convective by criterion 1. Figure 15b shows only 91.7 GHz PCT below 190 K, the 1% CDF of Tbs established by *Cecil et al.* [2005]. Here we see that strokes are located where convection is identified by the 190 K Tb threshold, but many strokes also occurred where convection was not identified. We conclude that the 190 K threshold for 91.7 GHz PCT is too strict a requirement for lightning in this case.

7. Discussion and Conclusions

We investigate lightning strokes and deep convection using data from WWLLN and passive microwave radiometer data from TMI and SSMIS. As expected and in agreement with studies at 37 and 85 GHz [e.g., *Liu et al.*, 2011], the scatterplots shown in Figures 2 through 6 show that lightning stroke rates and stroke probabilities increase with increasing Tb depressions for all frequencies examined (37–183.3 GHz). We note that *Liu et al.* [2011] found that stroke rates correlate better with the areal extent of cold Tbs rather than minimum Tb for TMI 37 and 85 GHz PCT. This is because, as they concluded, the convective area better quantifies the total amount of ice passing through the mixed-phase region in the convective core. *Liu et al.* [2011] used the TRMM pre-

cipitation feature database [*Liu et al.*, 2008], which finds contiguous pixels of nonzero rainfall in TMI level 2 data, to calculate the area of convective cores. Our results agree with *Liu et al.* [2011], and we would like to further examine stroke rate and cold Tb areas for WWLLN strokes and higher-frequency channels. Unfortunately, a similar precipitation database does not exist for SSMIS data, and thus the area of convective cores is beyond the scope of our analysis and not presented here. We plan to include cold Tb areas in our future work. In general, the results presented in Figures 2, 3, 4a, 4b, 5a, and 5b confirm and extend previous results by studying the

(a) SSMIS Tb$_{13}$ Criterion 1

(b) SSMIS 91.7 GHz PCT < 190 K

(c) WWLLN +/-15min.

Figure 15. SSMIS-F16/WWLLN case study over Mexico at ~1900 LT, 14 August 2010. (a) ΔT_{13} for 183.3 GHz Tbs that satisfy criterion 1 in section 2 from *Hong and Heygster* [2008] and (b) SSMIS 91.7 GHz PCT data below 190 K. (c) Lightning strokes (gray dots) for ±15 min of SSMIS pass time.

relationships between lightning rates and brightness temperatures or ice mass-related parameters [e.g., *Petersen et al.*, 2005; *Liu et al.*, 2011].

Maps in Figure 7 that require the 183.3 GHz channel criteria of *Hong and Heygster* [2008] (our equations (1) and (2)) and Figure 8 that require Tbs below 190 K in 85/91.7 GHz PCT channels show high probability of at least 1 stroke over well-established storm regions over land [e.g., *Cecil et al.*, 2005; *Petersen et al.*, 2005; *Zipser et al.*, 2006; *Liu et al.*, 2011] such as Central America, northern Argentina, coastal Australasia, southern China, southern United States, and Mexico. We find that the criteria used by Hong and Heygster select continental convective systems that are more likely to have at least one lightning stroke. The maps also indicate that convective systems over the oceans often have cold Tbs, but either do not produce lightning that is detected by WWLLN or have a lower probability of lightning when compared to systems over the land. These land/ocean differences agree with and complement the results of *Liu et al.* [2011] and earlier studies using TMI and LIS data. In general, our findings expand previous studies that investigated the connections between Tbs and deep convection, as well as links between these parameters and lightning.

The results presented in Figures 9 through 12 show a positive, although nonlinear, trend between lightning probabilities and dual-frequency Tb depressions. It follows that highly convective clouds contain a significant amount of large-sized frozen hydrometeors, which highlights the importance of the noninductive mechanism of cloud electrification. Moreover, in agreement with the maps in Figures 7 and 8, the dual-frequency plots show that convective systems over the ocean can have large Tb depressions that are not accompanied by lightning strokes. We apply a dual-frequency method similar to that used by *Wang et al.* [1997] using difference in 183.3 GHz channels. We see high lightning probabilities where Wang et al. and *Hong and Heygster* [2008] identified deep convection, namely, for 183.3 ± 1 GHz Tbs below about 200 K and ΔT_{13} values of about 5 to 25 K, with higher probabilities corresponding to lower values of 183.3 ± 1 GHz and ΔT_{13} Tbs over the land and coast. Wang et al. and Hong and Heygster associated such values with ice scattering. As in Figures 9 through 11, the land/ocean differences are also noticeable. Through a case study, we show that lightning stroke rates can be used to reconstruct microwave radiometer

Tbs for a thunderstorm in Mexico, and we demonstrate how the method of *Hong and Heygster* [2008] identifies stroke regions in this storm.

Our results have important implications for future applications of data from VLF lightning networks such as WWLLN. We argue that these networks can provide a similar picture of global convection related to Tbs as satellite lightning sensors such as LIS, even though VLF networks are biased toward strong lightning. Additionally, since low-Earth orbiting satellites like TRMM and DMSP/F16 only observe a particular region on Earth for a few minutes daily, VLF networks can potentially be used to fill in these microwave radiometer data gaps, as indicated by our case study. Radiometer data gaps are a noteworthy topic in meteorology, particularly while working with observations and forecasts of tropical cyclones. A few techniques address this problem by building visualization tools that use "morphing," which is "the digital manipulation of two or more images to make them appear to change into one another naturally to create time-continuous animations of irregular satellite images." For example, the Morphed Integrated Microwave Imagery at the Cooperative Institute for Meteorological Satellite Studies (MIMIC) tool inputs passive microwave imagery from multiple LEO satellite overpasses of a target tropical cyclone and displays a smoothly transitioned movie of the structure trends, which are important to the organization and intensity analysis [*Wimmers and Velden*, 2007]. As described by its developers, MIMIC can present some shortcomings as it uses wind advection to generate the image transition. MIMIC can potentially be improved by adding reconstructed Tbs from lightning rates, given that the quantitative uncertainties associated with this reconstruction method are taken into account.

Our study also helps quantify lightning as a proxy for deep convection and cloud hydrometeor distributions for future satellite lightning imagers such as the Geostationary Lightning Mapper (GLM) on the GOES-R/ GOES-S satellites (www.goes-r.gov). Ongoing and future analyses include examining seasonal and regional variations of relationships between WWLLN lightning and microwave radiometer data, as well as case studies of storm systems such as mesoscale convective systems and tropical cyclones [*Solorzano and Thomas*, 2015].

References

Abarca, S. F., K. L. Corbosiero, and T. J. Galarneau Jr. (2010), An evaluation of the Worldwide Lightning Location Network (WWLLN) using the National Lightning Detection Network (NLDN) as ground truth, *J. Geophys. Res.*, *115*, D18206, doi:10.1029/2009JD013411.

Bang, S. D., and E. J. Zipser (2015), Differences in size spectra of electrified storms over land and ocean, *Geophys. Res. Lett.*, *42*, 6844–6851, doi:10.1002/2015GL065264.

Bennartz, R., and P. Bauer (2003), Sensitivity of microwave radiances at 85–183 GHz to precipitating ice particles, *Radio Sci.*, *38*(4), 8075, doi:10.1029/2002RS002626.

Boccippio, D. J., S. J. Goodman, and S. Heckman (2000), Regional differences in tropical lightning distributions, *J. Appl. Meteorol.*, *39*, 2231–2248, doi:10.1175/1520-0450(2001)040<2231:RDITLD>2.0.CO;2.

Burns, B. A., X. Wu, and G. R. Diak (1997), Effects of precipitation and cloud ice on brightness temperatures in AMSU moisture channels, *IEEE Trans. Geosci. Remote Sens.*, *35*, 1429–1437.

Cecil, D. J. (2009), Passive microwave brightness temperatures as proxies for hailstorms, *J. Appl. Meteorol. Climatol.*, *48*, 1281–1286.

Cecil, D. J., and E. J. Zipser (2002), Reflectivity, ice scattering, and lightning characteristics of hurricane eyewalls and rainbands. Part II: Intercomparison of observations, *Mon. Weather Rev.*, *130*, 785–801.

Cecil, D. J., E. J. Zipser, and S. W. Nesbitt (2002), Reflectivity, ice scattering, and lightning characteristics of hurricane eyewalls and rain-bands. Part I: Quantitative description, *Mon. Weather Rev.*, *130*, 769–784.

Cecil, D. J., S. J. Goodman, D. J. Boccippio, E. J. Zipser, and S. W. Nesbitt (2005), Three years of TRMM precipitation features. Part I: Radar, radiometric, and lightning characteristics, *Mon. Weather Rev.*, *133*, 543–566.

Deeter, M. . N., and K. . F. Evans (2000), A novel ice-cloud retrieval algorithm based on the millimeter-wave imaging radiometer (MIR) 150- and 220-GHz channels, *J. Appl. Meteorol.*, *39*, 623–633.

Deierling, W., and W. A. Petersen (2008), Total lightning activity as an indicator of updraft characteristics, *J. Geophys. Res.*, *113*, D16210, doi:10.1029/2007JD009598.

Dowden, R. L., J. B. Brundell, and C. J. Rodger (2002), VLF lightning location by time of group arrival (TOGA) at multiple sites, *J. Atmos. Sol. Terr. Phys.*, *64*(7), 817–830, doi:10.1016/S1364-6826(02)00085-8.

Evans, K. F., and G. L. Stephens (1995), Microwave radiative transfer through clouds composed of realistically shaped ice crystals. Part II: Remote sensing of ice clouds, *J. Atmos. Sci.*, *52*, 2058–2072.

Hawkins, J. D., F. J. Turk, T. F. Lee, T. F. Lee, and K. Richardson (2008), Observations of tropical cyclones with the SSMIS, *IEEE Trans. Geosci. Remote Sens.*, *46*(4), 901–912, doi:10.1109/TGRS.2008.915753.

Holzworth, R. H., J. B. Brundell, M. McCarthy, K. Virts, M. L. Hutchins, A. R. Jacobson, and S. Heckman (2015), Variation in regional and global lightning, *American Geophysical Union Fall Meeting*, San Francisco, CA, AE12A-06. [Available at http://earthweb.ess.washington.edu/jnt/HolzworthAGU2015.pdf.]

Hong, G., and G. Heygster (2008), Intense tropical thunderstorms detected by the Special Sensor Microwave Imager/Sounder, *IEEE Trans. Geosci. Remote Sens.*, *46*(4), doi:10.1109/TGRS.2008.915750.

Hong, G., G. Heygster, J. Miao, and K. Kunzi (2005), Detection of tropical deep convective clouds from AMSU-B water vapor channels measurements, *J. Geophys. Res.*, *110*, D05205, doi:10.1029/2004JD004949.

Hutchins, M. L., R. H. Holzworth, J. B. Brundell, and C. J. Rodger (2012a), Relative detection efficiency of the World Wide Lightning Location Network, *Radio Sci.*, *47*, RS6005, doi:10.1029/2012RS005049.

Hutchins, M. L., R. H. Holzworth, C. J. Rodger, and J. B. Brundell (2012b), Far field power of lightning strokes as measured by the World Wide Lightning Location Network, *J. Atmos. Oceanic Technol.*, *29*, 1102–1110, doi:10.1175/JTECH-D-11-00174.1.

Jacobson, A. R., R. H. Holzworth, J. Harlin, R. L. Dowden, and E. H. Lay (2006), Performance assessment of the World Wide Lightning Location Network (WWLLN), using the Los Alamos Sferic Array (LASA) array as ground-truth, *J. Atmos. Oceanic Technol.*, *23*, 1082–1092, doi:10.1175/JTECH1902.1.

Jayaratne, E. R., C. P. R. Saunders, and J. Hallett (1983), Laboratory studies of the charging of soft hail during ice crystal interactions, *Q. J. R. Meteorol. Soc.*, *109*, 609–630.

Kodama, H., Y. Okabe, K. Tomisaka, Y. K. Kotono, and H. Kasuya (2007), Lightning frequency and microphysical properties of precipitating clouds over the western North Pacific during winter as derived from TRMM multisensor observations, *Mon. Weather Rev.*, *135*, 2226–2241.

Kummerow, C., W. Barnes, T. Kozu, J. Shiue, and J. Simpson (1998), The Tropical Rainfall Measuring Mission (TRMM) sensor package, *J. Atmos. Oceanic Technol.*, *15*, 809–817, doi:10.1175/1520-0426(1998)015<0809:TTRMMT>2.0.CO;2.

Lang, T. J., and S. A. Rutledge (2002), Relationships between convective storm kinematics, precipitation, and lightning, *Mon. Weather Rev.*, *130*, 2492–2506.

Latham, J., W. A. Petersen, W. Deierling, and H. J. Christian (2007), Field identification of a unique globally dominant mechanism of thunderstorm electrification, *Q. J. R. Meteorol. Soc.*, *133*, 1453–1457.

Lay, E. H., R. H. Holzworth, C. J. Rodger, J. N. Thomas, O. Pinto Jr., and R. L. Dowden (2004), WWLL global lightning detection system: Regional validation study in Brazil, *Geophys. Res. Lett.*, *31*, L03102, doi:10.1029/2003GL018882.

Leppert, K. D., II, and D. J. Cecil (2015), Signatures of hydrometeor species from airborne passive microwave data for frequencies 10–183 GHz, *J. Appl. Meteorol. Climatol.*, *54*, 1313–1334, doi:10.1175/JAMC-D-14-0145.1.

Liu, C., and E. J. Zipser (2008), Diurnal cycles of precipitation, clouds, and lightning in the tropics from 9 years of TRMM observations, *Geophys. Res. Lett.*, *35*, L04819, doi:10.1029/2007GL032437.

Liu, C., E. J. Zipser, D. J. Cecil, S. W. Nesbitt, and S. Sherwood (2008), A cloud and precipitation feature database from 9 years of TRMM observations, *J. Appl. Meteorol. Climatol.*, *47*, 2712–2728, doi:10.1175/2008JAMC1890.1.

Liu, C., D. Cecil, and E. J. Zipser (2011), Relationships between lightning flash rates and passive microwave brightness temperatures at 85 and 37 GHz over the tropics and subtropics, *J. Geophys. Res.*, *116*, D23108, doi:10.1029/2011JD016463.

Mansell, E. R., D. R. MacGorman, C. L. Ziegler, and J. M. Straka (2005), Charge structure and lightning sensitivity in a simulated multicell thunderstorm, *J. Geophys. Res.*, *110*, D12101, doi:10.1029/2004JD005287.

Muller, B. M., H. E. Fuelberg, and X. Xiang (1994), Simulations of the effects of water vapor, cloud liquid water, and ice on AMSU moisture channel brightness temperatures, *J. Appl. Meteorol.*, *33*, 1133–1154, doi:10.1175/15200450(1994)033<1133:SOTEOW>2.0.CO;2.

Nakamura, Y., et al. (2011), Global relationships between lightning and ice water path characteristics from WWLLN and AMSU-B/MHS, *Fifth Conf. on Meteo. Applic. of Lightning Data*, Seattle, Wash.

Nesbitt, S. W., and E. J. Zipser (2003), The diurnal cycle of rainfall and convective intensity according to three years of TRMM measurements, *J. Clim.*, *16*, 1456–1475.

Nesbitt, S. W., E. J. Zipser, and D. J. Cecil (2000), A census of precipitation features in the tropics using TRMM: Radar, ice scattering, and lightning observations, *J. Clim.*, *13*, 4087–4106.

Pessi, A., and S. Businger (2009), Relationships between lightning, precipitation, and hydrometeor characteristics over the North Pacific Ocean, *J. Appl. Meteorol.*, *48*, 833–848.

Petersen, W. A., H. J. Christian, and S. A. Rutledge (2005), TRMM observations of the global relationship between ice water content and lightning, *Geophys. Res. Lett.*, *32*, L14819, doi:10.1029/2005GL023236.

Peterson, M., C. Liu, D. Mach, W. Deierling, and C. Kalb (2015), A method of estimating electric fields above electrified clouds from passive microwave observations, *J. Atmos. Oceanic Technol.*, *32*, 1429–1446, doi:10.1175/JTECH-D-14-00119.1.

Price, C., M. Asfur, and Y. Yair (2009), Maximum hurricane intensity preceded by increase in lightning frequency, *Nat. Geosci.*, *2*, 329–332, doi:10.1038/NGEO477.

Reynolds, S. E., M. Brook, and M. F. Gourley (1957), Thunderstorm charge separation, *J. Meteorol.*, *14*, 163–178.

Rodger, C. J., J. B. Brundell, and R. L. Dowden (2005), Location accuracy of VLF World Wide Lightning Location (WWLL) network: Post-algorithm upgrade, *Ann. Geophys.*, *23*, 277–290.

Rodger, C. J., S. Werner, J. B. Brundell, E. H. Lay, N. R. Thomson, R. H. Holzworth, and R. L. Dowden (2006), Detection efficiency of the VLF World-Wide Lightning Location Network (WWLLN): Initial case study, *Ann. Geophys.*, *24*, 3197–3214.

Rodger, C. J., J. B. Brundell, R. H. Holzworth, and E. H. Lay (2009), Growing detection efficiency of the World Wide Lightning Location Network, in *Coupling of Thunderstorms and Lightning Discharges to Near-Earth Space: Proceedings of the Workshop*, edited by N. B. Crosby, T.-Y. Huang, and M. J. Rycroft, pp. 15–20, Am. Inst. Phys., Melville, New York, doi:10.1063/1.3137706.

Rosenfeld, D., and W. L. Woodley (2000), Convective clouds with sustained highly supercooled liquid water down to −37.5°C, *Nature*, *405*, 440–442, doi:10.1038/35013030.

Rudlosky, S. D., and D. T. Shea (2013), Evaluating WWLLN performance relative to TRMM/LIS, *Geophys. Res. Lett.*, *40*, 1–5, doi:10.1002/grl.50428.

Schols, J. L., J. A. Weinman, G. D. Alexander, R. E. Stewart, L. J. Angus, and A. C. L. Lee (1999), Microwave properties of frozen precipitation around a North Atlantic Cyclone, *J. Appl. Meteorol.*, *38*, 29–43, doi:10.1175/1520-0450(1999)038<0029:MPOFPA>2.0.CO;2.

Solorzano, N. N., and J. N. Thomas (2015), WWLLN lightning and passive satellite microwave data: Typhoon evolution and intensity change, *Asia Oceania Geosciences Society*, *12th Annual Meeting*, Singapore, AS03-A041. [Available at http://earthweb.ess.washington.edu/jnt/Solorzano_AOGS_2015.pdf.]

Spencer, R. W., W. S. Olson, R. Wu, D. W. Martin, J. A. Weinman, and D. A. Santek (1983), Heavy thunderstorms observed over land by the Nimbus 7 scanning multichannel microwave radiometer, *J. Climate Appl. Meteorol.*, *22*, 1041–1046, doi:10.1175/1520-0450(1983)022<1041:HTOOLB>2.0.CO;2.

Staelin, D. H., and F. W. Chen (2000), Precipitation observations near 54 and 183 GHz using the NOAA-15 satellite, *IEEE Trans. Geosci. Remote Sens.*, *38*(5), 2322–2332.

Takahashi, T. (1984), Thunderstorm electrification—A numerical study, *J. Atmos. Sci.*, *41*, 2541–2558.

Thomas, J. N., N. N. Solorzano, S. A. Cummer, and R. H. Holzworth (2010), Polarity and energetics of inner core lightning in three intense North Atlantic hurricanes, *J. Geophys. Res.*, *115*, A00E15, doi:10.1029/2009JA014777.

Toracinta, E. R., and E. J. Zipser (2001), Lightning and SSM/I-ice-scattering mesoscale convective systems in the global tropics, *J. Appl. Meteorol.*, *40*, 983–1002.

Toracinta, E. R., D. J. Cecil, and E. J. Zipser (2002), Radar, passive microwave, and lightning characteristics of precipitating systems in the tropics, *Mon. Weather Rev.*, *130*, 802–824.

Virts, K. S., J. M. Wallace, M. L. Hutchins, and R. H. Holzworth (2013), Highlights of a new ground-based, hourly global lightning climatology, *Bull. Am. Meteorol. Soc.*, *94*, 1381–1391, doi:10.1175/BAMS-D-12-00082.1.

Vivekanandan, J., J. Turk, and V. N. Bringi (1991), Ice water path estimation and characterization using passive microwave radiometry, *J. Appl. Meteorol.*, *30*, 1407–1421.

Wang, J. R., J. Zhan, and P. Racette (1997), Storm-associated microwave radiometric signatures in the frequency range of 90–220 GHz, *Atmos. Oceanic Technol.*, *14*, 13–31, doi:10.1175/1520–0426(1997)014<0013:SAMRSI>2.0.CO;2.

Wiens, K. C., S. A. Rutledge, and S. A. Tessendorf (2005), The 29 June 2000 supercell observed during STEPS. Part II: Lightning and charge structure, *J. Atmos. Sci.*, *62*, 4151–4177, doi:10.1175/JAS3615.1.

Wimmers, A. J., and C. S. Velden (2007), MIMIC: A new approach to visualizing satellite microwave imagery of tropical cyclones, *Bull. Am. Meteorol. Soc.*, *88*(8), 1187–96.

Wu, R., and J. A. Weinman (1984), Microwave radiances from precipitating clouds containing aspherical ice, combined chase, and liquid hydrometeors, *J. Geophys. Res.*, *89*, 7170–7178, doi:10.1029/JD089iD05p07170.

Yan, B., and F. Weng (2009), Assessments of F16 Special Sensor Microwave Imager and Sounder antenna temperatures at lower atmospheric sounding channels, *Adv. Meteor.*, doi:10.1155/2009/420985.

Zipser, E. J., D. J. Cecil, C. Liu, S. W. Nesbitt, and D. P. Yorty (2006), Where are the most intense thunderstorms on Earth?, *Bull. Am. Meteorol. Soc.*, *87*, 1057–1071.